Simulating the acoustic response of cavities to improve microphone array measurements in closed test section wind tunnels

Simulating the acoustic response of cavities to improve microphone array measurements in closed test section wind tunnels

Colin VanDercreek, Francesco Avallone, Daniele Ragni, et al.

Citation: The Journal of the Acoustical Society of America **151**, 322 (2022); doi: 10.1121/10.0009274
View online: https://doi.org/10.1121/10.0009274
View Table of Contents: https://asa.scitation.org/toc/jas/151/1
Published by the Acoustical Society of America

JASA ARTICLE

Simulating the acoustic response of cavities to improve microphone array measurements in closed test section wind tunnels

Colin VanDercreek,[a] Francesco Avallone,[b] Daniele Ragni,[c] and Mirjam Snellen[d]
Faculty of Aerospace Engineering, Delft University of Technology, Kluyverweg 1, 2629 HS Delft, The Netherlands

ABSTRACT:
Cavities placed along wind tunnel walls can attenuate the turbulent boundary layer (TBL) fluctuations as they propagate into the cavity. Placing microphones within the cavities can thus improve the signal-to-noise ratio of acoustic data. However, standing waves form within these cavities distorting the acoustic measurements. This work uses a finite element (FE) solver to evaluate how cavity geometry (depth, diameter, and wall angle) and wall material (hard-walled and melamine foam) affect the amplitude and eigenfrequency of standing waves when excited by an incident acoustic plane wave. Good agreement between predicted and measured acoustic transfer functions is shown. Compared to cylindrical cavities, countersunk and conical cavities improve the overall response, i.e., reducing the quality factor quantifying the resonance and damping characteristics. Stainless steel coverings also reduce the quality factor. A finding is that the shape of the external foam holder rather than the cavity shape drives the standing wave characteristics for the melamine foam cavities. The optimization problem of minimizing the acoustic response while also attenuating the TBL is thus decoupled by using the melamine foam. Consequently, these considerations can be addressed independently by optimizing the outer cavity shape for acoustics and the melamine foam insert for TBL attenuation.
https://doi.org/10.1121/10.0009274

(Received 28 May 2021; revised 8 November 2021; accepted 17 December 2021; published online 20 January 2022)
[Editor: David E. Scarborough] Pages: 322–333

I. INTRODUCTION

Acoustic array measurements on the wall of closed test section wind tunnels are affected by turbulent boundary layer (TBL) hydrodynamic pressure fluctuations. When their levels are higher than those of the signal of interest, the resulting low signal–to–noise ratio (SNR) hinders source identification and quantification. There are two complementary approaches to improve the SNR. The first is to use beamforming with an array of microphones.[1] The array intrinsically reduces the influence of incoherent TBL pressure fluctuations by using the microphones integral to the array to perform beamforming which identifies coherent (over the microphones) acoustic sources. This reduces but does not eliminate the effect of the incoherent TBL pressure fluctuations. Applying beamforming post-processing techniques such as removing the diagonal of the cross-spectral matrix (CSM), using other imaging methods such as CLEAN-SC,[2] or performing principal component analysis on the CSM[3] further reduces the TBL noise contribution. However, these techniques cannot detect sources more than 20 dB below that of the TBL noise level, depending on the microphone array configuration.[4] The second technique is to place the microphones within cavities embedded in wind tunnel walls. Cavities improve the SNR by attenuating the TBL hydrodynamic fluctuations at the microphone location.[5–7] The attenuation of TBL pressure fluctuations is dependent on several geometrical parameters. Specifically, the cavity depth,[7,8] diameter,[9] and presence of a countersink[7,8] have been shown to influence the measured TBL spectra. Furthermore, covering the cavities with an acoustically transparent material such as Kevlar[5,10] or a finely woven stainless steel cloth[8] has been shown to reduce the TBL spectra levels further by approximately 10 dB compared to the same cavity without a covering. Although there are a significant number of studies focusing on the noise radiated from cavities,[11–13] there are limited studies on the impact of cavity geometry on acoustic measurements made with microphones placed within the cavities. The cavity shape determines the frequencies at which standing waves occur and the amplitude of the resulting spectral peaks. In addition to amplifying the acoustic signal, cavities can distort the signal by attenuating it. This article describes a simulation framework for improving cavity designs for wind tunnel acoustic measurements.

The standing waves, also referred to as quarter–wavelength modes, and the resulting amplification occur

[a]Electronic mail: c.p.vandercreek-1@tudelft.nl, ORCID: 0000-0003-2869-8124.
[b]ORCID: 0000-0002-6214-5200.
[c]ORCID: 0000-0002-8014-5650.
[d]ORCID: 0000-0002-6579-5655.

https://doi.org/10.1121/10.0009274

when the incident acoustic wave and the wave reflecting off the cavity bottom constructively coincide, at a frequency near the cavity's quarter-wavelength mode harmonic frequency. The cavity geometry (depth, diameter, wall angle), boundary materials, and fluid properties determine these harmonic frequencies. Ideally, the cavities should have a negligible effect on the acoustic wave with thus minimal distortion of the acoustic measurements.

Figure 1 illustrates typical acoustic and hydrodynamic responses for a given cavity geometry. The change in sound pressure level (ΔL_p) between measurements taken at the bottom of the cavity and flush with the wall is used to derive this response. A typical covered cavity attenuates the TBL noise, illustrated by the dashed line, with increasing frequency, thus improving the overall SNR.[14] However, the same cavity distorts the acoustic signal by introducing a standing wave centered at a specific frequency, as shown by the solid line. This standing wave amplifies the measured sound level, introducing errors into the acoustic measurements, and must be accounted for when processing data.

The focus of this article is on how the geometry of the cavity affects its acoustic response. Acoustic plane waves emanating from a far-field acoustic source were simulated using the multiphysics simulation software package COMSOL. The propagation of plane waves into different cavity shapes is studied. The acoustic propagation is simulated without background flow and assumes linear acoustics with no thermoviscous acoustics effects present. The cavity radiation acoustics dominate the thermoviscous acoustics for larger aspect ratio cavities, such as those examined in this study. The latter thus do not contribute significantly to the overall response. Since the effect of the cavity on the plane wave measurements should have minimum attenuation or amplification on the far-field signal of interest, it is important to identify how the acoustic transfer function between the incident plane wave and the acoustic response at the cavity bottom is affected by the cavity geometry. Three families of cavity shapes are studied to understand the effect of geometry on the response. First, this study investigates cylindrical cavities of different depths and diameters. The overall acoustic response of cylindrical cavities is, for example, also investigated in Ref. 15. Second, this work investigates the effect of different countersink angles on a cylinder of constant depth. Last, a conical cavity with varied wall angles is investigated. For all cavities, the aperture is simulated with and without a stainless-steel cloth covering. The cavity walls were simulated as either perfectly reflecting or sound-absorbing using a porous model for melamine foam. A finding of this study is a suggested method of cavity design, where optimizing the balance between the acoustic and hydrodynamic response is no longer necessary. These responses can be addressed independently through the use of sound-absorbing melamine.

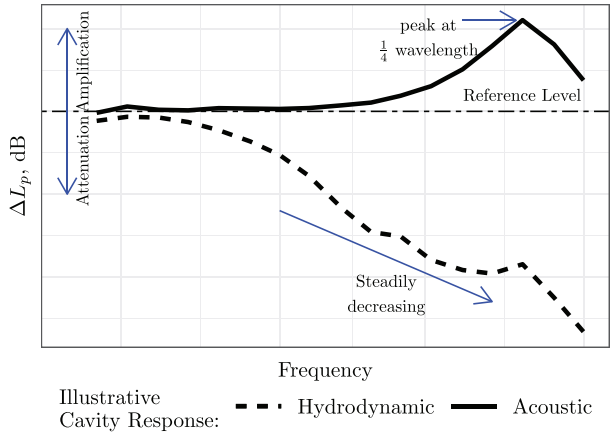

FIG. 1. (Color online) Example illustrating the effect a cavity has on the incident acoustic wave and the TBL pressure fluctuations.

This paper is structured as follows: Sec. II describes the simulation assumptions, defines the geometric parameters, and evaluates the simulation convergence. Section III compares the simulated cavity results with experimental data as well discusses how the acoustic cavity response can be treated as independent of the TBL flow. Section IV quantifies the effect of cavity depth, diameter, stainless steel cloth covering, wall angle, sound absorbing melamine material, and plane wave incident angle on the acoustic response. Section V summarizes the major findings of this paper.

II. NUMERICAL SETUP

The COMSOL multiphysics simulation software package is used to simulate the incident plane wave, its propagation into a cavity, and its subsequent reflection. The *Pressure Acoustics Frequency Domain* interface, which is part of the *Acoustics Module*, uses a finite element (FE) solver to solve the Helmholtz equation. The Helmholtz equation, shown in Eq. (1), where c is the speed of sound, p is the acoustic pressure, and ω is the angular frequency, governs the propagation of acoustic waves through a constant density fluid in the frequency domain,[16]

$$\nabla \cdot (\nabla p) + \frac{\omega^2}{c^2} p = 0. \tag{1}$$

In this work we neglect thermoviscous effects because the cavity diameters and acoustic wavelengths of interest are significantly larger than the thermal and viscous boundary layers.[17] As a result, radiation acoustics are dominant for these large aspect ratio cavities.

Figure 2 defines the geometric parameters for the three families of cavities considered in this paper. These shapes are representative of the cavities used in practice. Figure 2(a) is the straight-walled cylindrical cavity with depth L, and aperture radius a being equal to the bottom radius b. The radius, b, is 0.005 m based on previous experimental work[9,14] using cavities of this size to study their effect on TBL attenuation. The ideal cavity diameter for TBL attenuation is application specific. The countersunk family of cavities is shown in Fig. 2(b). For this cavity, b is the radius of the cavity bottom, and a is the aperture radius. Figure 2(c) shows the conical cavity, where b is the radius of the conical frustrum, a is the aperture radius, x_0 is the distance from the

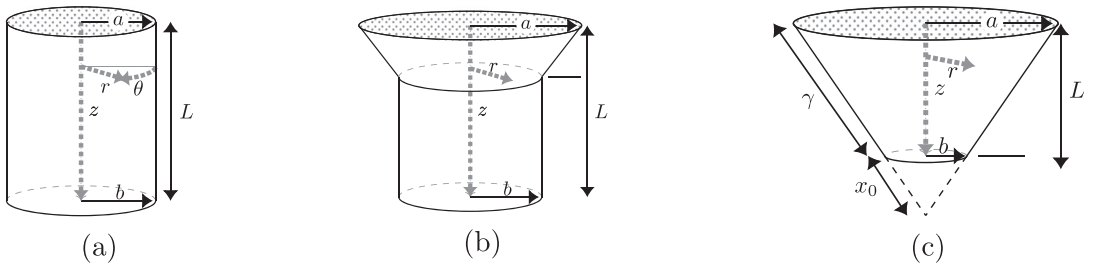

FIG. 2. Generic cavity shapes considered in the experiment and FE studies: (a) straight-walled cylindrical cavity, (b) cylindrical cavity with countersink, (c) conical cavity. Parameters r, z, and θ are the cylindrical coordinates. a is the aperture radius, b is the bottom radius, L is the cavity depth, ψ is the wall angle, and x_0 is the distance from the conical vertex to the frustrum.

frustrum to the imaginary vertex. The conical cavities are truncated at the location of the microphone. The cavity depth, for all cavities, is defined by L, nominally 0.01 m. For the countersunk and conical cavities, the wall angle is defined by ψ with $\psi = 90°$ being the straight-walled cylinder case. The countersunk cavity features a straight wall from the bottom of the cavity to $z = 2L/3$.

A. Model setup

Figure 3 illustrates the three-dimensional computational domain. A symmetric boundary condition divides the domain in half to reduce computational time. This plane is perpendicular to the acoustic wave front. A cylindrical perfectly matched layer (PML) simulates an open boundary by absorbing all outgoing wave energy. It imposes a complex-valued coordinate transformation in the domain so that the energy of the waves that enter the PML region decays rapidly.[17] The quarter-arc cylinder shape eliminates discontinuities at the boundary between the PML and the pressure acoustics domain. This shape ensures that the PML mesh elements remain isotropic to avoid spurious reflections. Periodic boundary conditions, defined using the Floquet periodicity condition, are placed on the left and right sides of the domain. This allows for non-normal ($\phi > 0°$) incident pressure waves to enter and leave the domain with no spurious reflections.

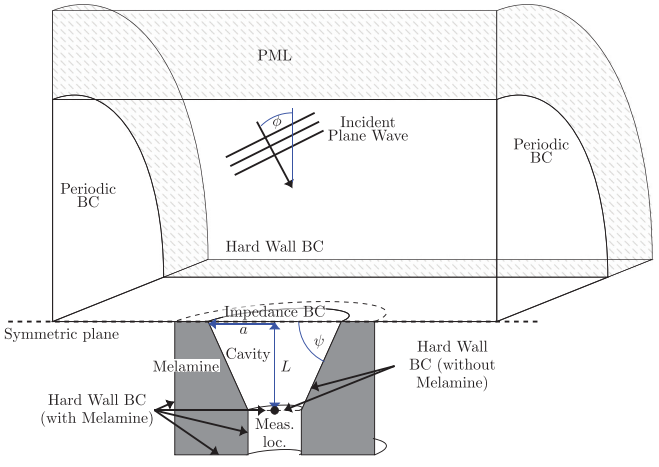

FIG. 3. (Color online) COMSOL computational domain setup where ϕ is the incident plane wave angle, ψ is the countersunk/conical cavity wall angle, L is the cavity depth, and r is the radius of the cavity with a value a at the top and b at the bottom. The light shaded region is the perfectly matched layer (PML).

The incident plane wave is modeled as a background pressure field within the quarter cylinder region. The plane wave is defined by Eq. (2) where p_0 is the wave amplitude, $\mathbf{x}$ is the wave position vector, k the wavenumber, and $\mathbf{e_k}$ is the wave direction unit vector. For this simulation, the plane wave amplitude was held constant with respect to frequency at 1.0 Pa and the frequency was varied between 0.25 and 105 kHz,

$$p = p_0 \exp\left[-ik\left(\frac{\mathbf{x}\cdot\mathbf{e_k}}{|\mathbf{e_k}|}\right)\right]. \tag{2}$$

The top of the cavity is either open or defined by an interior impedance boundary condition. The latter accounts for the stainless steel covering. The measured normalized acoustic impedance, Z, of the stainless steel cloth is 0.15. The normalization is with respect to the characteristic acoustic impedance of air, z_0 which is defined as ρc^2. The cloth has 200 threads per cm^2 and is 0.05 mm thick. The Netherlands Aerospace Centre (NLR) measured the cloth impedance in their impedance tube for this research. The plane surrounding the cavity represents the wind tunnel wall and is a hard wall boundary condition.

The cavities are either modeled as shown in Fig. 2 or out of melamine as shown in Fig. 3. For the cases without melamine, the cavity walls are defined as perfectly reflecting hard walls. For the melamine foam cavities, the foam is a poroacoustics region with a radius of 2.25 cm and a depth of 4.5 cm with the cavity formed at the top. The Johnson-Champoux-Allard (JCA) semi-empirical poroacoustic model is used. Table I lists the porous matrix properties for Basotec TG melamine[18] used in this paper. The properties are as follows: ϵ_p is the material porosity, R_f is the flow resistivity, the viscous characteristic length is L_v, the thermal characteristic length is L_{th}, and τ_∞ is the tortuosity factor.

The computational domain is meshed using a combination of tetrahedral elements and swept elements. The

TABLE I. Melamine porous matrix properties for the Johnson-Champoux-Allard semi-empirical model.

ϵ_p	R_f, Pa s m^{-2}	L_v, m	L_{th}, m	τ_∞
0.993	9297.6	2.12×10^{-4}	4.35×10^{-4}	1.0133

https://doi.org/10.1121/10.0009274

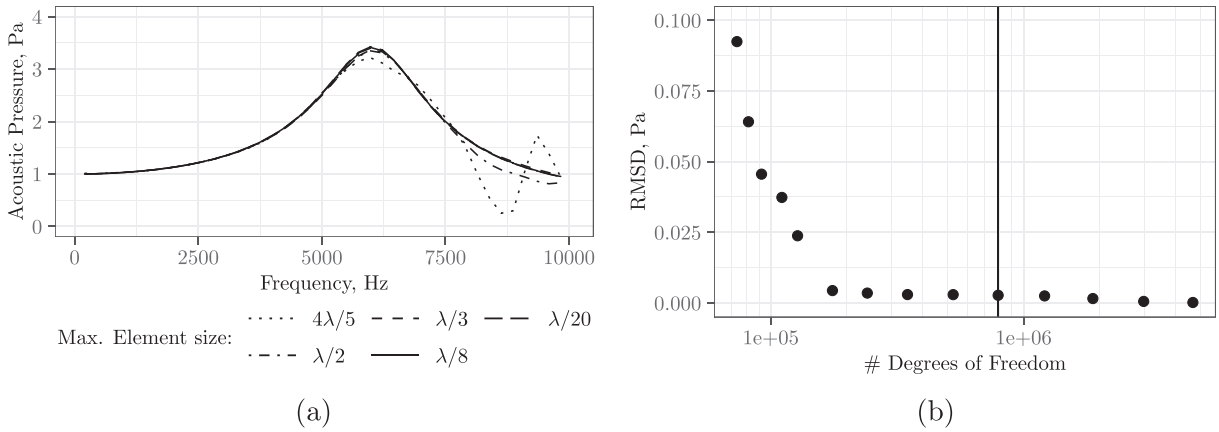

FIG. 4. Mesh convergence on the: (a) Acoustic pressure at the bottom of a cylindrical cavity with respect to the mesh element size upper limit, defined by the fractional size of the acoustic wavelength at 10 kHz. $\lambda/8$ (4.3×10^{-3} m) is the mesh size upper limit used in this paper. (b) Root mean square deviation (RMSD) between the pressure of different meshes and the solution for the finest mesh ($\lambda/20$). Plotted with respect to the number of degrees of freedom (DoF) in the simulation for a given mesh size. The vertical line is the $\lambda/8$ case.

tetrahedral elements are used everywhere except for the PML. The PML uses isotropic swept elements to minimize spurious reflections. The maximum mesh element size is $\lambda/8$, where λ is the wavelength of the highest frequency studied, 10 kHz. The resulting element size upper limit is 4.3×10^{-3} m. Figure 4(a) shows the acoustic response at the bottom of a cylindrical cavity for five different mesh sizes. As this figure shows, once the maximum mesh size approaches $\lambda/8$, the solution converges. Figure 4(b) shows the root mean square deviation (RMSD) of the cavity acoustic response. The RMSD is the difference between the solution for the finest mesh and the solution for the coarser meshes. The vertical line is the RMSD for the $\lambda/8$ case (10 kHz acoustic wave). These figures show that choosing a maximum element size of $\lambda/8$ is sufficient for an accurate solution.

B. Cases modelled

The cavity depth (L), bottom radius (b), covering, wall angle (ψ), and wall material were varied to study the relationship between cavity geometry and the quarter–wavelength mode characteristics. Table II lists the geometrical parameters that were studied. The radii and cavity depths for the countersunk and conical cavities were chosen to match the cavities used in a prior experiment.[14] Additionally, the incident plane wave angle ϕ was varied between 0° and 90° for the cylindrical and conical cavities.

III. MODEL VALIDATION

A. Description of the measurements

The experimental data used to validate this work originated from a previous experimental campaign[14] studying the effect of cavity geometry on beamforming measurements. In that campaign, 16 cavities were installed in a 1.1 m×0.4 m poly-carbonate plate covered with the 200 threads per cm^2 (#500) stainless steel cloth as described previously. The 16 cavities are interchangeable and installed in 5 cm diameter holes. A flush-mounted microphone is placed in the center of the array. The three cavity shapes of Fig. 2 were tested with the stainless steel cloth covering. The cylindrical and countersunk cavities have poly-carbonate walls and the conical cavity is cut out of a melamine foam cylindrical insert.

Only measurement data from one cavity position is used to validate the work of this paper, since the acoustic response was found to be independent of cavity location. The acoustic signal was generated by a Visaton K 50 SQ speaker, mounted at a distance 0.8 m normal to the flat plate containing the cavities. The speaker has a baffle diameter of 4.5 cm. The speaker emitted white noise with an overall sound pressure level ($L_{p,overall}$), measured at the plate location without flow, of 64 dB.

G.R.A.S. 40PH analog free-field microphones were used. This microphone features an integrated constant current power (CCP) amplifier and a 135 dB dynamic range. Each microphone has a diameter of 7 mm and a length of 59.1 mm. All the microphones were calibrated individually using a *G.R.A.S. 42AA* pistonphone following the guidelines of Mueller.[19] The transducers have a flat frequency response within ±1 dB from 50 Hz to 5 kHz and within ±2 dB from 5 to 20 kHz. The data acquisition system consists of a *National Instruments* (NI) *PXIe-4499* sound and vibration module with 24–bit resolution. The board is controlled by a NI *RMC-8354* computer *via* a NI *PXIe-8370* board. The

TABLE II. Simulated cavity geometric parameters.

Cavity	Depth (L), mm	Radius (b), mm	Angle (ψ), °	Covered	Wall Material
Cylindrical	5, 10, 15, 20, 30	5, 10	90	Yes, No	Hard, Melamine
Countersunk	10	5	80, 70, 60, 45, 30, 20, 10	Yes, No	Hard, Melamine
Conical	10	5	80, 70, 60, 45, 30, 20, 10	Yes, No	Hard, Melamine

sampling frequency of the recordings was 51.2 kHz. The signal was sampled for a duration of 45 s. The spectra are calculated using Welch's method with 1024 samples with a 50% overlap using Hanning windowing with a resulting frequency resolution of 50 Hz.

B. Comparing simulated and measured acoustic transfer functions

The acoustic transfer function is defined as the difference between the decibel scale spectra of the flush and cavity bottom microphone measurements. This is equivalent to dividing the cavity spectra by the flush spectra at each frequency before converting to a decibel scale. The spectral responses are calculated using Welch's method. 6 dB is added to the transfer functions to account for the difference between the free-field and flush measurements since flush measurements feature a doubling of the pressure due to the reflection off of the flat plate. Two hard-walled cavities (cylindrical and countersunk) and one conical cavity formed out of melamine foam were simulated and compared with experimental data. Figure 5 shows the SPL deviation, ΔL_p, from the expected free-field measurement for these cavities. The simulations (dashed lines) agree closely with the experimental data (solid lines). The hard-walled cylindrical and countersunk cavities match the predicted standing wave amplitude as well as the frequency of their respective peaks: 6.3 kHz for the straight-walled case and 7.0 kHz for the countersunk case. The fluctuations in the experimental data below 5.0 kHz are hypothesized to be due to the flush reference microphone being offset slightly from the cavity in the experimental measurements as well as reflections from the wind tunnel exit nozzle. Figure 5 also shows that the JCA porous prediction is close to the measured response of the melamine cavity. The melamine conical cavity simulation data matches the trends in the experimental data with at most a 4 dB difference in predicted amplitude near 5 kHz due to a frequency shift between the model and experiment. This difference could be reduced with the application of a different porous model. These results give confidence that the simulation results, analysis, and conclusions presented in this paper are accurate.

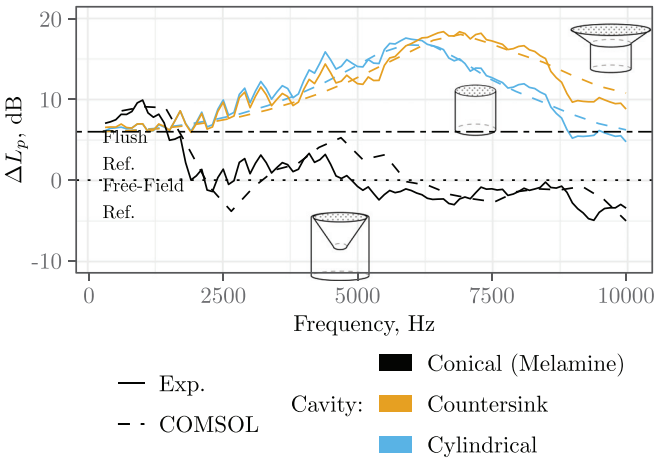

FIG. 5. (Color online) The simulated and experimental acoustic transfer functions between the cavity bottom and flush measurements are shown for three cavities. The cavities are two hard-walled cavities (countersunk and cylindrical) and a conical cavity made of melamine foam. ΔL_p is the deviation from the free-field, $\Delta L_p = 0$ corresponds to the expected free-field spectra level.

C. Independence of acoustic and hydrodynamic response

This work assumes that the acoustic response of the cavities is not influenced by the presence of a TBL. This assumption of independence is based on insight gained from Ref. 14 in which an acoustic source was measured with a turbulent boundary layer present over the microphone array. Figure 6(a) shows the spectra of the measurements for either the acoustic source or the TBL being present. Figure 6(b) shows the summation of these spectra (dotted line), and also the measurements obtained with the two sources (TBL and acoustic) being present simultaneously (long-short dashed line). A close agreement per cavity geometry between the lines in Fig. 6(b) is observed. A maximum deviation of 3 dB is seen between 1 and 3 kHz in Fig. 6(b). This close agreement between the two suggests that the acoustic signal at the microphone can be considered to be independent of the flow over the cavities for the frequency range of interest (0.25 to 10.0 kHz). This assumption is key to applying this acoustic analysis to cavities used in a closed test section wind tunnel with flow present.

IV. ANALYSIS OF RESULTS

The goal of this study is to quantify how cavity shape, the presence of a stainless steel cloth, and wall material affect acoustic measurements at the cavity bottom. The geometric characteristics and the boundary conditions (e.g., fluid properties) determine the amplitude and frequency of the quarter–wavelength cavity modes. The cavity depth, diameter, covering, countersink angle, conical wall angle, and wall material were varied to find the relationship between geometry and the quarter-wavelength mode frequencies, f_n, and amplification, quantified by the quality factor Q, which will be defined at the end of Sec. IV A. The fluid properties and other boundary conditions are held constant for this analysis.

A. Effect of cavity depth and diameter

The response of cylindrical cavities to an incident plane wave was simulated for several cavity depths and diameters. Figures 7 and 8(a) show the resulting acoustic response (ΔL_p) with respect to the free-field levels and the simulated flush microphone reference levels. The latter measurements are approximately 6 dB higher than the free-field due to the doubling of the incident pressure wave amplitude at the wall.

The cylindrical cavity depths range from 0.005 to 0.03 m and their radii vary from 0.005 and 0.01 m. The incident plane wave frequencies are between 0.25 and 10 kHz.

https://doi.org/10.1121/10.0009274

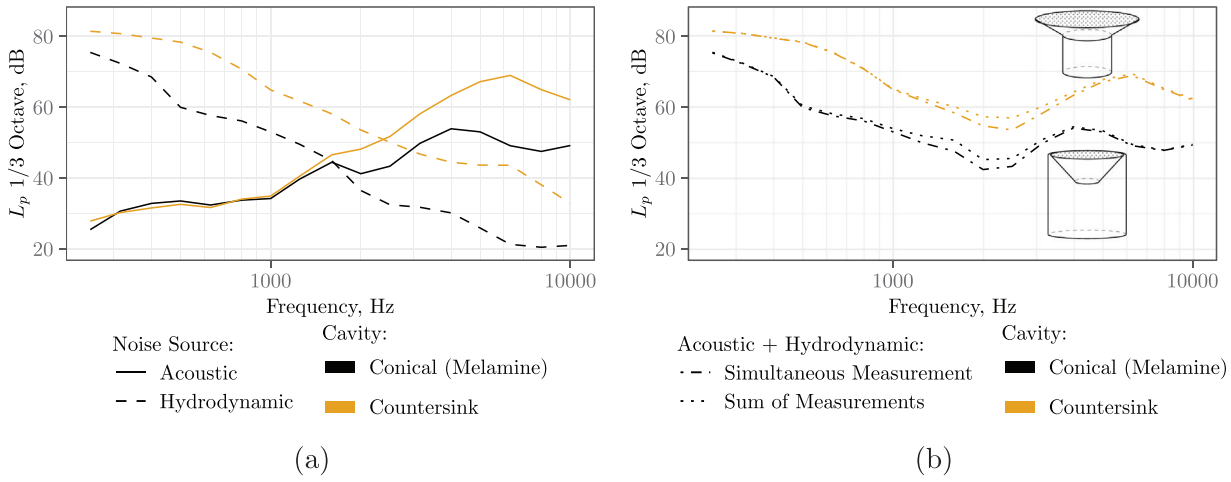

FIG. 6. (Color online) (a) Independent cavity microphone measurements with only an acoustic source and with only the TBL ($U_\infty = 20\,\mathrm{ms}^{-1}$) present over two cavities. (b) Comparison of the measurement of the acoustic source with the TBL present and the sum of the independent measurements.

ΔL_p is plotted with respect to both frequency in Fig. 7 and the non-dimensional Helmholtz number (He)in Fig. 8(a). Figure 7 shows how with decreasing cavity depth, L, the peak frequency increases. Also, with decreasing diameter for the same depth, the peak frequency increases. Figure 8(a) shows that when normalizing by He, the peaks collapse to the same value of He. The Helmholtz number is defined as follows: $He = L_{\mathrm{eff}}\omega/c$, where ω is the angular frequency and c the speed of sound. L_{eff} is the cavity depth plus a correction term for the cavity diameter which is discussed later in this section.

The peaks in Fig. 8(a) are from an acoustic mode within the cavity. While longitudinal, radial, and azimuthal[16] modes can be present, it is the longitudinal mode that appears in Fig. 8(a). The longitudinal mode is also referred to as a depth mode, and is the quarter–wavelength mode[16] as mentioned previously. These modes form standing waves in the longitudinal direction of the cavity. Standing waves occur when an acoustic wave reflects at a change in impedance (e.g., a duct opening or cavity bottom) and the resulting reflection constructively interferes with another incident wave. This results in peaks[20] at odd-numbered harmonics.

To understand why these peaks are only due to the longitudinal modes, it is useful to evaluate the cavity in terms of the pressure field for a circular duct. Applying the principles of duct acoustics[21,22] shows this to be the case. At the cavity aperture, the incidence pressure wave must match the pressure field at the aperture of the cavity. This pressure field at the cavity aperture can be decomposed into radial and azimuthal mode shapes. These modes propagate in the longitudinal direction into the cavity. However, for the cavity diameters (≈ 0.01 m) and frequencies (≤ 10 kHz) in this study, the higher-order radial and azimuthal modes, referred to by their mode numbers $m > 0$ and $\mu > 1$ do not propagate as they are cut-off. Equation (3), where a is the cavity aperture radius and $\alpha_{m\mu}$ is the radial wavenumber, defines this cut-off condition,

$$\frac{\omega a}{c} > \alpha_{m\mu}. \tag{3}$$

As an example, assuming a cavity diameter of 0.01 m and using the first Bessel derivative root whose value is $\alpha_{m=1,\mu=1} = 1.8412$, Eq. (3) states that the first non-planar mode will only propagate for frequencies above 20.1 kHz. Further details can be found in the description of a previously developed analytical model.[22] The resulting planar mode propagates in the longitudinal direction. The reflection of this wave off of the cavity bottom interferes constructively with the incident wave at the harmonic frequency, resulting in a peak. Since the quarter–wavelength mode is the dominant mode, this analysis will focus on how the cavity geometry affects this mode's harmonic frequency and amplification.

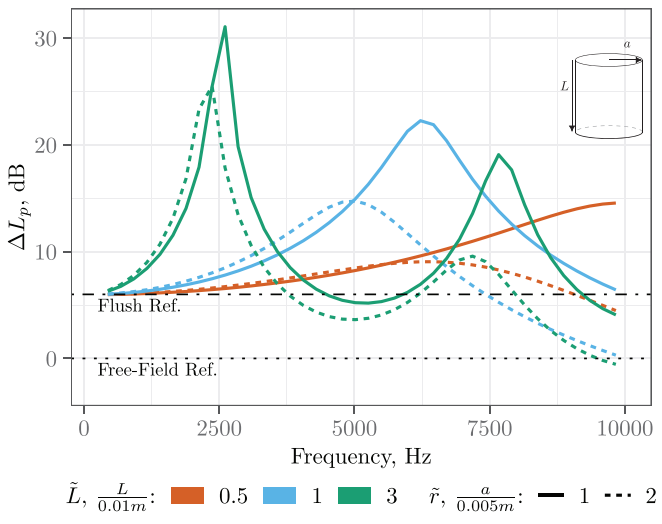

FIG. 7. (Color online) ΔL_p values with respect to the free-field for different normalized cylindrical cavity depths ($\tilde{L} = L/0.01\mathrm{m}$) and radii ($\tilde{r} = a/0.005\mathrm{m}$). The solid lines represent the responses for $a = 0.005$ m. The dashed lines represent the responses for $a = 0.01$ m. The horizontal dash-dotted and dotted lines represent the flush and free-field responses, respectively. The cavities feature hard walls with no stainless steel cloth covering.

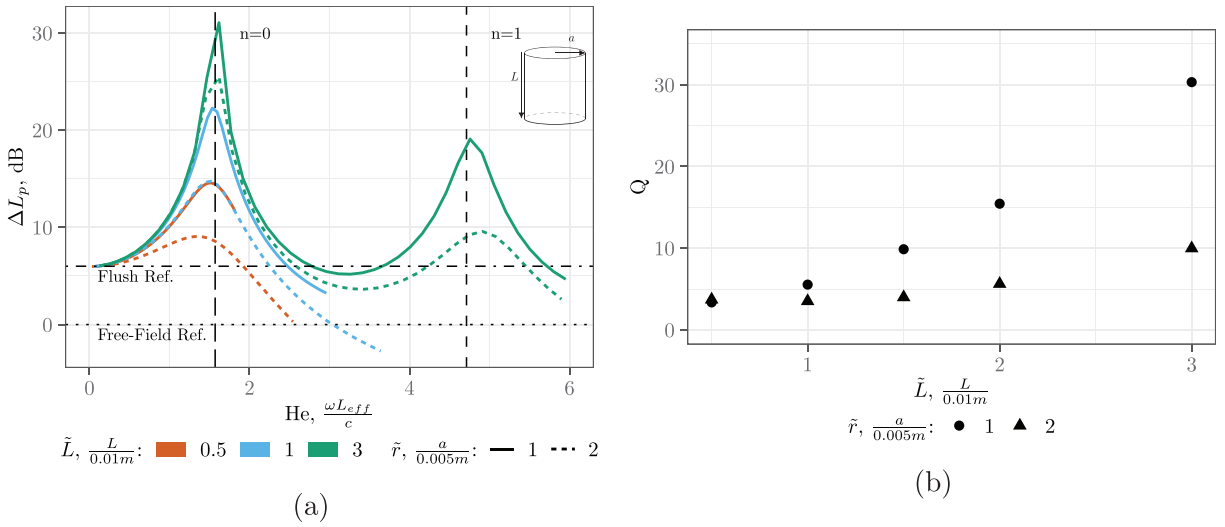

FIG. 8. (Color online) (a) ΔL_p values with respect to the free-field for different normalized cylindrical cavity depths ($\tilde{L}$) and radii ($\tilde{r}$). The dimensions are normalized with respect to $L = 0.01$ m and $r = 0.005$ m. The cavities feature hard walls with no stainless steel cloth covering. The horizontal dash-dotted and dotted lines represent the flush and free-field responses, respectively. (b) The effect of cavity depth and diameter on the quality factor (Q).

For straight-walled cavities, Eq. (4) predicts the harmonic frequency f_n, where n is the mode number and L_{eff} is the effective cavity depth. The effective depth, L_{eff}, is the depth of the cavity, L, with a depth correction term, δ, applied. This correction term accounts for the radiation impedance of the open end.[23] The radiation impedance is dependent on the cavity diameter, covering, frequency, and whether or not it is flanged or unflanged,

$$f_n = \frac{(2n+1)c}{4L_{\text{eff}}}. \tag{4}$$

For a cavity in a wall, the wall is treated as an infinite flange. The depth correction, δ, for an infinitely flanged opening is defined in Eq. (5),[23] where k is the wavenumber and a is the cavity aperture radius, see Fig. 2(a). For the cavities of interest, δ ranges between $0.597a$ and $0.707a$,

$$\delta = 0.8216a\left[1 + \frac{(0.77ka)^2}{1 + 0.77ka}\right]^{-1}. \tag{5}$$

Figure 7 shows that increasing the cavity diameter, while holding depth constant, reduces the harmonic frequency. This shift increases for larger aspect ratio (a/L) cavities because δ increases L_{eff}. According to Eqs. (4) and (5) the standing wave peak locations collapse to $He = \pi/2$ for the fundamental mode, see Fig. 8(a). The vertical dashed lines in Fig. 8(a) are the fundamental mode ($n = 0$) and the first harmonic ($n = 1$) predictions made with Eq. (4). Applying this equation shows that the cavities with highest values of f_n are the shallowest with the smallest diameter (e.g., $\tilde{L} = L/0.01\,\text{m} = 0.5$ and $\tilde{r} = a/0.005\,\text{m} = 1$), as shown in Fig. 7. The deeper the cavity, the lower values of f_n (e.g., $\tilde{L} = 3$). The amplitudes also depend on cavity depth and diameter. The deeper the cavity, the higher the amplitude of the standing wave while the larger the aspect ratio, the lower the amplification.

The effect of cavity geometry on the amplification is quantified by the quality factor, Q, shown in Fig. 8(b). Q is defined as the ratio between the real and imaginary components of the eigenfrequency, ζ, of the standing wave; $Q = \text{Re}(\zeta)/\text{Im}(\zeta)$. The quality factor is also calculated by $Q = f_n/(f_u - f_l)$, where f_u and f_l are the upper and lower frequencies at the 1/2 power location, defined as 3 dB below the peak harmonic. Thus, Q describes the amplitude and width of the standing wave spectral peak. The higher the value of Q, the greater the amplification, which is undesirable. Figure 8(b) shows that Q increases both with increasing cavity depth and with decreasing diameter. This effect is more pronounced when the depth is significantly larger than the diameter. For example, the $\tilde{L} = 3$ case Q drops from 30 to 10 when the diameter is doubled while at $\tilde{L} = 1$ the reduction drops by approximately 2, from 5 to 3. This trend does not hold for shallow cavities. Cavities with the same aspect ratio have similar harmonic amplification. This is seen for the cavities where $\tilde{L} = 1$, $\tilde{r} = 2$ and $\tilde{L} = 0.5$, $\tilde{r} = 1$ in Fig. 8(a). Figure 8(b) also shows that Q is close for these two cavities as well as for the cavities with $\tilde{L} = 2$, $\tilde{r} = 2$ and $\tilde{L} = 1$, $\tilde{r} = 1$.

These results show that a deep cylindrical cavity is undesirable for acoustic measurements due to the high Q and due to the presence of multiple harmonics. Shorter and wider cavities are more desirable for acoustic measurements as the standing wave amplitudes are minimized and shifted to higher frequencies. Ideally, the harmonic frequencies of the standing waves would be higher than the upper range of the frequency of interest (10 kHz), however, this is not feasible for the cavity geometries that attenuate the TBL noise contribution. For example, applying Eq. (4), a 1.0 cm diameter cavity, would have to have a depth of 0.52 cm, which would limit its effectiveness in reducing the TBL noise contribution compared to a deeper cavity. The optimal cavity depth for improving acoustic measurements by reducing the TBL noise at the microphone is application dependent.

https://doi.org/10.1121/10.0009274

B. Effect of stainless steel cloth covering

Placing a stainless steel cloth or Kevlar on top of the cavity reduces the TBL fluctuations at the microphone,[5,10] however one area of concern is its effect on the acoustic signal. Simulations were run for the straight-walled cavities with an impedance boundary condition at the top of the cavity, as discussed previously in Sec. II A. Figure 9(a) shows the effect of this impedance on the peak locations and amplitudes for the same cavities. The cloth reduces the location of the peak from a *He* of 1.55 to 1.50 for $\tilde{L} = 1$ and from 1.57 to 1.55 for $\tilde{L} = 3$ ($\Delta f = 0.2$ kHz). The effect of the cloth on the location of the peak is small due to its normalized acoustic impedance of 0.15 being smaller than the radiation impedance of an infinitely flanged cylindrical cavity. The radiation impedance of the cavity opening can be estimated using the reflection coefficient R, Eq. (6), in the expression for normalized radiation impedance Z_r Eq. (7),[24] where $Z_c = 1/\pi a^2$ is the impedance of the cavity,

$$R(\omega) = -\frac{1 - 0.182ika}{1 - 1.825ika + 0.649(ika)^2}, \tag{6}$$

$$Z_r = Z_c \frac{1+R}{1-R}. \tag{7}$$

For the case of the cylindrical cavity where $\tilde{L} = 1$ and $\tilde{r} = 1$, the estimated normalized radiation impedance (Z_r) is 1948.

The stainless steel cloth's effect on Q is greater than its effect on the frequency of f_n. Figure 9(b) shows that the stainless steel cloth reduces Q for the same cavities. The deeper the cavity, the larger the reduction in Q, for example for the $\tilde{L} = 3$ case, Q drops from 30.3 to 4.5. while for the $\tilde{L} = 1$ case, the effect is less dramatic with Q decreasing from 5.5 to 2.8. The transmission loss through the cloth is calculated to be approximately 1 dB. From these simulations, it is apparent that a low impedance covering, such as the fine stainless steel mesh, improves the acoustic response of the cavity by reducing the amplitude of the quarter–wavelength modes with minimal transmission loss.

Section IV A showed that larger aspect ratio cavities (larger diameters and shorter depths) are more desirable, i.e., they have lower values of Q than low aspect ratio cavities. However, a stainless steel cloth covering allows for the cavity depth to be increased, reducing the TBL noise, while minimizing the amplification due to the quarter–wavelength mode.

C. Effect of wall angle

Figure 10(a) shows the effect of different countersink wall angles on the acoustic response of a countersunk cavity covered with a stainless steel cloth. The angle ψ was varied from a shallow angle, $\psi = 10^\circ$ to the straight-walled case, $\psi = 90^\circ$, in 10° increments. Additionally, a 45° countersunk cavity was simulated to match experimental data. The depth of the cavities, L, was held constant and is the same as the $\tilde{L} = 1$ cases simulated previously. The response for different values of ψ is plotted versus the Helmholtz number. δ is calculated using the aperture radius a shown in Fig. 2(b) and Eq. (5). For the steeper angles, $\psi \geq 70^\circ$, the harmonic frequency agrees with the predictions using Eq. (4), shown by the vertical dashed line. As the angle decreases, the values of f_n increase compared to the straight–walled cavity. The effect of ψ on the harmonic peak, quantified by Q is shown in Fig. 10(b). As ψ decreases, Q decreases. This dependence is more significant for the cases without a stainless steel cloth. Without this covering, Q decreases from 5.6 for the straight–walled case to 2.6 for $\psi = 10^\circ$. With the cloth, the amplitude of the standing wave is damped and Q decreases from 2.9 to 2.6 with decreasing ψ.

The acoustic responses of conical cavities with the stainless steel cloth covering, are shown in Fig. 11(a). These cavities were simulated at the same wall angles, depth, and radius at the frustrum (b) as the countersunk cavities. The Helmholtz number was calculated using $L_{\text{eff}} = L + \delta$ with δ

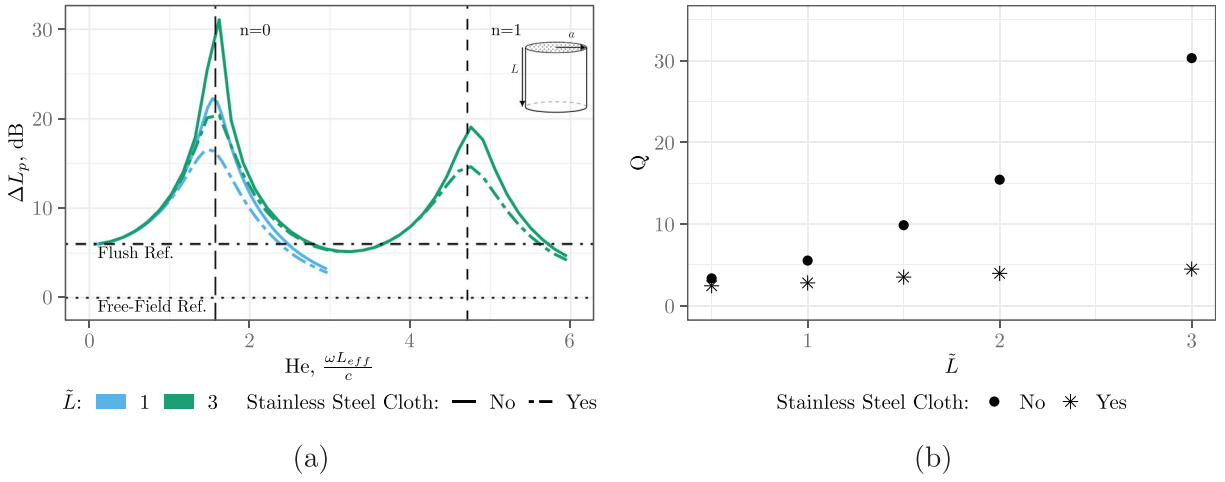

FIG. 9. (Color online) (a) Effect of stainless steel cloth on ΔL_p values with respect to the free-field for selected normalized cylindrical cavity depths $\tilde{L} = L/0.01$ m and $\tilde{r} = a/0.005$ m $= 1$. The cavities are cylindrical with hard walls. The horizontal dash-dotted and dotted lines represent the flush and free-field responses, respectively. (b) The effect of the stainless steel cloth on the quality factor, Q, for cylindrical cavities of different depths.

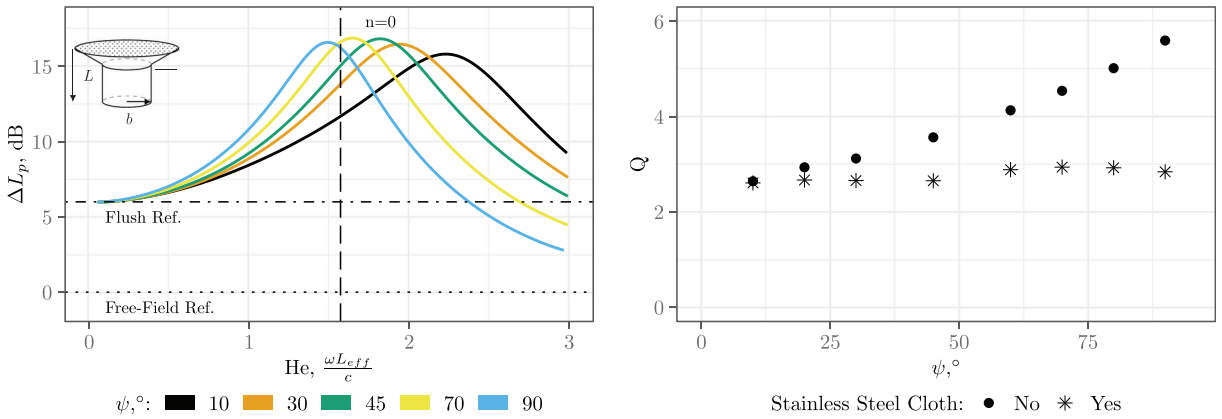

FIG. 10. (Color online) (a) ΔL_p for different countersink angles (ψ) with respect to the free-field and flush cases. Cavities have a normalized depth $\tilde{L} = L/0.01\,\text{m} = 1$ and $\tilde{r} = b/0.005\,\text{m} = 1$, the countersink depth is $\tilde{L}/3$. All cavities have a stainless steel cloth covering. (b) Quality factor for different countersink angles (ψ) with and without a stainless steel cloth.

being calculated in the same manner as the countersunk cases. Decreasing ψ decreases the harmonic amplitude, even with the stainless steel cloth covering in contrast to the countersunk cases. The harmonic frequency increases slightly with respect to the straight-walled case for $\psi \geq 70°$. For shallower angles, f_n can be estimated by solving the transcendental equation, Eq. (8). Here, k is the wavenumber, x_0 is the distance between the bottom frustum and the conical vertex, and γ is the length of the cavity sidewall, i.e., the distance between the vertex and the aperture,[25] see Fig. 2(c). The resulting harmonic frequencies do not occur at integer values of the fundamental frequency but are spaced at slightly monotonically increasing intervals, depending on x_0,

$$\tan(k\gamma) = -kx_0. \tag{8}$$

The predictions made with Eq. (8) agree with the simulation for $\psi < 45°$. As an example, the prediction for $\psi = 10°$ is shown in Fig. 11(a). For steeper angles, f_n is over predicted. This is presumably due to the lack of a correction term for the infinite flange at the opening for conical waveguides.[25]

Figure 11(b) shows that decreasing ψ has a greater effect on Q than for the countersunk cavities. From $\psi = 90°$ to $\psi = 10°$, Q drops from 5.5 to 1.0 for the case without the cloth covering. With the covering, Q drops from 2.8 to 1.0. Below $\psi = 50°$, the stainless steel cloth has minimal effect on the harmonic response of the cavity.

The ideal cavity should have the fundamental standing wave harmonic frequency higher than the highest frequency of interest. Barring that, its response should be as flat as possible. From these simulations, it is clear that cavities with angled sides perform better by having a lower harmonic amplitude than the equivalent straight-walled cylindrical cavity. Conical cavities feature a flatter response than countersunk cavities. For conical cavities with shallow angles, $\psi \leq 10°$, the cavity response approaches that of the flush wall. However, at these angles, the cavity is less effective at attenuating the TBL because the TBL will stay attached to

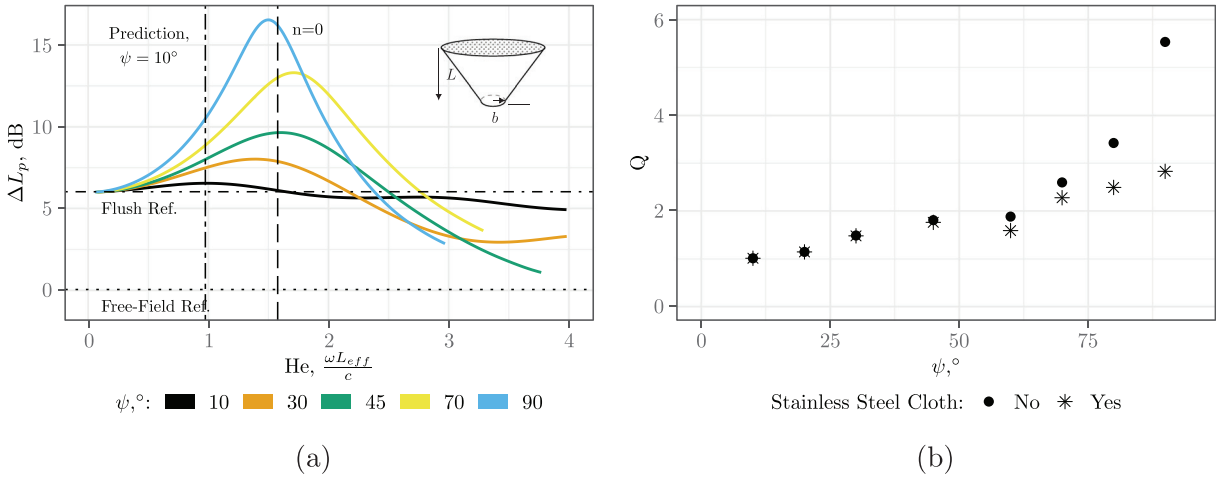

FIG. 11. (Color online) (a) ΔL_p for different conical angles with a stainless steel cloth covering (ψ) with respect to the free-field and flush cases. Cavities have a normalized depth $\tilde{L} = L/0.01\,\text{m} = 1$ and $\tilde{r} = b/0.005\,\text{m} = 1$. Also, shown is the analytical prediction for the harmonic frequency for $\psi = 10°$. (b) Quality factor for different conical angles (ψ) with and without a stainless steel cloth.

https://doi.org/10.1121/10.0009274

the cavity walls and the response will be similar to that of the flush case. However, the limiting value of ψ depends on the TBL properties and will be application-dependent. Having a low wall angle limits the depth of the cavity because the beamforming array limits the cavity aperture size. This limit is due to the microphone spacing requirements. Therefore, conical cavities should have wall angles between 10° and 45°.

D. Effect of melamine walls

Cavities formed out of melamine foam attenuate TBL noise more than hard walled cavities, as was observed in previous work.[14] Therefore, this study evaluates the effect of this sound absorbing material on the standing wave amplitudes and harmonic frequencies within cavities. The JCA porous acoustic model was used to simulate the melamine foam. The model parameters are described in Table I. All cavities considered in this section share the same outer construction with only the inner cavity (made out of melamine) shape changing. An example of this can be seen in Fig. 12, where the exterior of the cavities is a cylinder and the interior a cone. The normalized depth of this cylinder is $\tilde{L} = 4.3$ and its normalized radius is $\tilde{r} = 4.5$. The outer surface is modeled as a hard walled boundary condition. The top of the cavity is simulated with the stainless steel cloth covering. Three inner melamine cavities were studied: two cylindrical cavities and a conical cavity. The cylindrical ones have normalized depths of $\tilde{L} = 1$ and $\tilde{L} = 3$ with a normalized radius of $\tilde{r} = 1$. The conical one has a wall angle $\psi = 30°$ and a depth of $\tilde{L} = 1.2$. As a baseline comparison, a solid block of foam was also considered, in other words, without any interior cavities present.

Figure 12(a) shows the acoustic responses measured at the bottom of the two cylindrical cavities and the conical cavity. As a comparison, the measurement from the top of the solid cylindrical foam block is included. Compared to the hard wall cavities, Figs. 8(a)–11(a), the melamine reduces the amplitude of the standing waves harmonic amplitudes and no strong peaks are present. When comparing the conical cavity and the cylindrical cavity, which have similar depths ($\tilde{L} = 1.2$ and $\tilde{L} = 1$), it is apparent that the cavity shape has minimal influence on the acoustic spectral response. In order to determine if the acoustic response is primarily influenced by the measurement location along the z-axis and not the cavity shape, the response measured at different locations along the z-axis within the solid foam block is shown with dashed lines in Fig. 12(b). The locations chosen correspond to the depths of the three cavities ($z = \tilde{L}$), which are shown with solid lines. It is clear that the responses, ΔL_p, are similar which suggests that the interior cavity shape has minimal influence on the acoustic response. Instead, the measurement location within the cylindrical foam block drives the response. In other words, the acoustic response within the foam is driven by the shape of the outer cylindrical cavity, $\tilde{L} = 4.3$, $\tilde{r} = 4.5$, formed by the hard backing walls surrounding the foam insert and not the cavity cut out of the foam. Applying Eq. (4) to the outer shape of the melamine foam and substituting the speed of sound in the porous medium for the speed of sound in air, gives reasonable agreement with the simulation results, shown by the vertical dashed lines in Fig. 12(a). The speed of sound in the melamine JCA porous model is calculated as follows: $c = \sqrt{K(\omega)/\rho_{\text{rig}}(\omega)}$,[26] where K is the equivalent bulk modulus and ρ_{rig} is the equivalent rigid density which are determined from the material properties in Table I.

The shape and material of the foam insert can be optimized to minimize the standing wave amplifications using the guidelines for depth and wall angle previously discussed. The cavity shape cut into the foam can thus be optimized independently to minimize the turbulent boundary layer pressure fluctuations at the microphone. Figure 6(a), as an example, shows that a conical shape in the melamine reduces the hydrodynamic TBL noise significantly while Fig. 7 shows the impact on the acoustic signal is minimal. Therefore, the problems of optimizing the cavities for

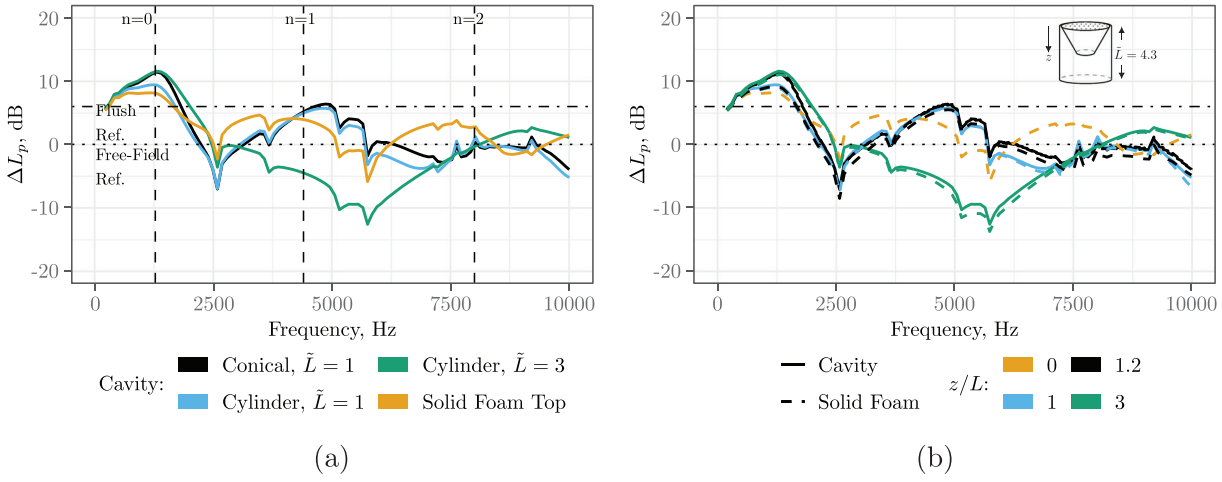

FIG. 12. (Color online) (a) Acoustic response (ΔL_p) of cavities made of melamine foam: Conical ($\psi = 30°$, $\tilde{L} = 1.2$), cylindrical ($\tilde{L} = 1$ and $\tilde{L} = 3$, $\tilde{r} = 1$), cylindrical foam insert ($\tilde{L} = 4.3$ and $\tilde{r} = 4.5$). (b) ΔL_p at different depths (z) within the foam insert, represented by the dashed lines compared to cavities of equivalent depth, represented by the solid lines.

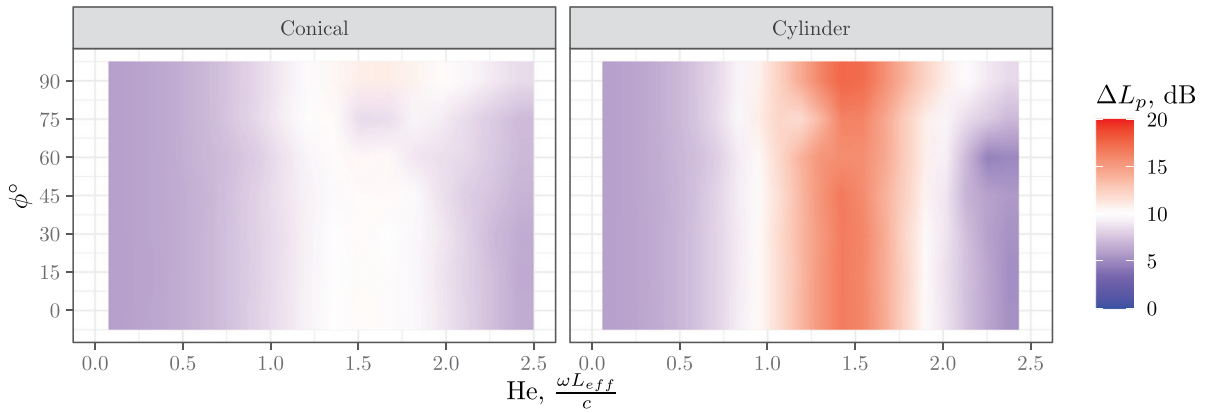

FIG. 13. (Color online) Acoustic response for conical cavity with $\psi = 45^\circ$ and the straight walled cavity for incidence angles (ϕ) from 0° to 90°. The cavities feature hard walls with no stainless steel cloth covering.

minimizing the distortion of acoustic measurements and optimizing the cavities to maximize the attenuation of the TBL noise can potentially be decoupled.

E. Effect of incidence angle

The microphone arrays used for beamforming can be several meters in diameter. Therefore, the incidence angle, ϕ, of the acoustic waves varies across the array. Only the cavities aligned with the acoustic source of interest have an incident wave angle close to 90°. To evaluate the dependence of the cavity acoustic response on the incident angle, the incidence angle was varied from 0° to 90°. A conical cavity ($\psi = 45^\circ$) and a straight-walled cylindrical cavity, both with depths of $\tilde{L} = 1$ were simulated. The resulting acoustic response (ΔL_p) is shown in Fig. 13. As this figure shows, the straight-walled cavity has a minimal change in its response for the range of ϕ. The conical cavity shows a small amount of variation of approximately 3 dB at ϕ around 75°. The standing waves excitation can thus be treated as independent of the incident far-field wave angle.

V. CONCLUSIONS

This paper quantifies the effect of different cavity shapes and materials on the acoustic response at the bottom of a cavity. The COMSOL multiphysics software package was used to simulate the acoustic response of cylindrical, countersunk, and conical cavities. Cavity depth, diameter, and wall angles were systematically varied. This article also quantifies the influence of a stainless steel cloth covering. The cavities were simulated as both hard-walled and with melamine foam walls. The results of the simulation matched the experimental measurements for the hard-walled cavities. The JCA poroacoustic model, used to model the melamine foam, agreed with the experimental trends but additional studies are necessary to rectify the frequency shift observed.

The longitudinal quarter–wavelength modes are the dominant acoustic phenomena present in the cavity. To minimize distortion of the acoustic signals, the frequency of the quarter–wavelength modes should be as high as possible with the amplitude as low as possible. For cylindrical cavities this frequency decreases with increasing cavity depth. Increasing the cavity diameter reduces the amplitude of these standing waves while slightly decreasing their harmonic frequency. Cavities with the same depth to diameter ratio have similar quality factors, Q, which quantifies the amount of amplification. Adding a stainless steel cloth covering reduces the harmonic frequency by approximately $2\% - 5\%$ while reducing the amplification significantly. For the conical and countersunk cavities, changing the countersink angle and wall angle further reduced the standing wave amplitude. The response was found to be independent of the incident plane wave angle. Forming the cavities out of a melamine foam insert showed that the acoustic response of the cavity is driven by the shape of its hard-walled outer construction, with the interior cavity shape having minimal influence. This finding is important because instead of designing one cavity to attenuate the turbulent boundary layer (TBL) pressure fluctuations while also minimizing the strength of the standing waves, these constraints can be optimized separately.

Specifically, a conical outer shape with a low acoustic impedance covering can minimize the influence of standing waves. The conical shape reduces the amplitude of standing waves compared to an equivalent cylindrical cavity, while the covering further reduces the strength of these waves. The inner foam cavity can thus be designed to maximise the attenuation of the TBL. The work presented here supports optimizing cavity shapes for wind tunnel acoustic measurements as well as understanding the acoustic performance of existing ones.

ACKNOWLEDGMENTS

This work is part of the research program THAMES with project No. 15215, which is (partly) financed by the Dutch Research Council (NWO). The authors would also like to acknowledge the THAMES project partners for their insight and assistance.

[1]Y. Liu, A. R. Quayle, A. P. Dowling, and P. Sijtsma, "Beamforming correction for dipole measurement using two-dimensional microphone arrays," J. Acoust. Soc. Am. **124**(1), 182–191 (2008).

[2]P. Sijtsma, R. Merino-Martinez, A. M. Malgoezar, and M. Snellen, "High-resolution CLEAN-SC: Theory and experimental validation," Int. J. Aeroacoust. **16**(4-5), 274–298 (2017).
[3]S. Amailland, J.-H. Thomas, C. Pézerat, and R. Boucheron, "Boundary layer noise subtraction in hydrodynamic tunnel using robust principal component analysis," J. Acoust. Soc. Am. **143**(4), 2152–2163 (2018).
[4]P. Sijtsma, "Accuracy criterion for source power integration with CSM diagonal removal," in *8th Berlin Beamforming Conference*, Berlin, Germany (2020), pp. 1–15.
[5]S. Jaeger, W. Horne, and C. Allen, "Effect of surface treatment on array microphone self-noise," in *6th AIAA/CEAS Aeroacoustics Conference and Exhibit*, American Institute of Aeronautics and Astronautics, Lahaina, HI (2000).
[6]H.-C. C. Shin, W. R. Graham, P. Sijtsma, C. Andreou, and A. C. Faszer, "Implementation of a phased microphone array in a closed-section wind tunnel," AIAA J. **45**(12), 2897–2909 (2007).
[7]V. Fleury, L. Coste, R. Davy, A. Mignosi, C. Cariou, and J. M. Prosper, "Optimization of microphone array wall mountings in closed-section wind tunnels," AIAA J. **50**(11), 2325–2335 (2012).
[8]A. Carballo-Crespo and K. Takeda, "An investigation of microphone array installation effects," in *47th AIAA Aerospace Sciences Meeting*, Orlando, FL (2009).
[9]C. P. VanDercreek, A. Amiri-Simkooei, M. Snellen, and D. Ragni, "Experimental design and stochastic modeling of hydrodynamic wave propagation within cavities for wind tunnel acoustic measurements," Int. J. Aeroacoust. **18**(8), 752–779 (2019).
[10]M. C. Remillieux, E. D. Crede, H. E. Camargo, R. A. Burdisso, W. J. Devenport, M. Rasnick, P. V. Seeters, A. Chou, P. Van Seeters, and A. Chou, "Calibration and demonstration of the new Virginia Tech anechoic wind tunnel," in *14th AIAA/CEAS Aeroacoustics Conference (29th AIAA Aeroacoustics Conference)* (2008).
[11]K. K. Ahuja and J. Mendoza, "Effects of cavity dimensions, boundary layer, and temperature on cavity noise with emphasis on benchmark data to validate computational aeroacoustic codes," NASA Contractor Report No. 4653, NASA (1995).
[12]G. Kooijman, A. Hirschberg, and J. Golliard, "Acoustical response of orifices under grazing flow: Effect of boundary layer profile and edge geometry," J. Sound Vib. **315**(4), 849–874 (2008).
[13]A. T. De Jong, H. Bijl, A. Hazir, and J. Wiedemann, "Aeroacoustic simulation of slender partially covered cavities using a Lattice Boltzmann method," J. Sound Vib. **332**(7), 1687–1703 (2013).
[14]C. P. VanDercreek, R. Merino-Martínez, P. Sijtsma, M. Snellen, R. Merino-Martinez, P. Sijtsma, and M. Snellen, "Evaluation of the effect of microphone cavity geometries on acoustic imaging in wind tunnels," Appl. Acoust. **181**, 108154 (2021).
[15]M. J. Casiano and S. R. Fischbach, "Analytical and numerical modeling of sensor port acoustics," in *TP-20210000024*, NASA Marshall Space Flight Center, Huntsville, AL (2021).
[16]P. M. Morse and K. U. Ingard, *Theoretical Acoustics* (McGraw-Hill, New York, 1968).
[17]COMSOL, "Acoustics module user's guide," in COMSOL Multiphysics, v. 5.5 (COMSOL, Stockholm, Sweden, 2019).
[18]N. Kino, T. Ueno, Y. Suzuki, and H. Makino, "Investigation of non-acoustical parameters of compressed melamine foam materials," Appl. Acoust. **70**(4), 595–604 (2009).
[19]T. J. Mueller, *Aeroacoustic Measurements* (Springer, Berlin, 2002), p. 313.
[20]C. D. Field and F. R. Fricke, "Theory and applications of quarter-wave resonators: A prelude to their use for attenuating noise entering buildings through ventilation openings," Appl. Acoust. **53**(1-3), 117–132 (1998).
[21]A. Rona, "The acoustic resonance of rectangular and cylindrical cavities," J. Algorithms Comput. Technol. **1**(3), 329–356 (2007).
[22]C. P. VanDercreek, P. Sijtsma, M. Snellen, D. Ragni, F. Avallone, and D. G. Simons, "Deterministic model of acoustic wave propagation in a cavity," in *25th AIAA/CEAS Aeroacoustics Conference*, American Institute of Aeronautics and Astronautics, Delft, The Netherlands (2019).
[23]J. P. Dalmont, C. J. Nederveen, and N. Joly, "Radiation impedance of tubes with different flanges: Numerical and experimental investigations," J. Sound Vib. **244**(3), 505–534 (2001).
[24]F. Silva, P. Guillemain, J. Kergomard, B. Mallaroni, and A. N. Norris, "Approximation formulae for the acoustic radiation impedance of a cylindrical pipe," J. Sound Vib. **322**(1-2), 255–263 (2009).
[25]G. P. Scavone, "An acoustic analysis of single-reed woodwind instruments with an emphasis on design and performance issues and digital waveguide modeling techniques," Doctoral thesis, Stanford University, Stanford, CA (1997).
[26]J. F. Allard and N. Atalla, *Propagation of Sound in Porous Media: Modelling Sound Absorbing Materials*, 2nd ed. (Wiley-Blackwell, Oxford, 2009), pp. 1–358.